heritage

MDPI

Article

Inside the Sarcophagus: Non-Destructive Testing of a Medieval Tomb in the Cathedral of Bamberg (Germany)

Roland Linck [1,2,*], Johanna Skrotzki [3,4], Andreas Stele [1], Tatjana Hecher [1] and Jörg W. E. Fassbinder [2]

[1] Geoscientific Prospection, Bavarian State Department for Monuments and Sites, Hofgraben 4, 80539 Munich, Germany; andreas.stele@blfd.bayern.de (A.S.); tatjana.hecher@blfd.bayern.de (T.H.)
[2] Department for Earth and Environmental Sciences, Institute for Geophysics, Ludwig-Maximilians-University Munich, Theresienstr. 41/IV, 80333 Munich, Germany; joerg.fassbinder@lmu.de
[3] Main Scientific Laboratory, Bavarian State Department for Monuments and Sites, Hofgraben 4, 80539 Munich, Germany; johanna.skrotzki1@smail.th-koeln.de
[4] Cologne Institute of Conservation Sciences, Cologne University of Applied Sciences, Ubierring 40, 50678 Cologne, Germany
* Correspondence: roland.linck@blfd.bayern.de

Abstract

In recent years, digital technologies have become increasingly prevalent in the field of heritage protection. In addition to geomatic techniques like laser scanning (LiDAR) and Structure-from-Motion (SfM), geophysical methods, especially Ground-Penetrating Radar (GPR), offer added value for investigating protected buildings and objects. Additionally, chemical analysis (e.g., X-ray fluorescence, XRF) and mineral magnetic methods can be utilized to investigate specific research topics. All these methods are completely non-invasive and leave the heritage site untouched. Furthermore, they are cost-efficient and fast to use. Within this paper, we want to present an integrated study of a medieval sarcophagus in Bamberg Cathedral. The geophysical surveys via GPR and magnetic susceptibility (MS) measurements should answer open questions regarding the construction and internal layout of the sandstone sarcophagus, dated to the Early or High Middle Ages. The susceptibility data indicated an inner lead coffin in the lower part behind the stone slabs due to an unusual diamagnetic response in these parts. In contrast, the GPR data gave no such indication and revealed that the interior is too small for a direct burial of the bishop. Hence, an additional XRF survey was conducted to help solve this contradiction. The latter data indicate that the lead could be due to remains of a former painting on the sarcophagus with colours containing lead white pigments. Due to the porous sandstone, the moist environmental conditions, and the high weight of the lead elements, these could have accumulated at the bottom of the sarcophagus, creating the diamagnetism detected by the magnetic susceptibility measurements.

Keywords: non-destructive testing; NDT; ground-penetrating radar; GPR; magnetic susceptibility prospection; X-ray fluorescence; XRF; apple LiDAR; sarcophagus; white lead

Check for updates

Academic Editor: Wenke Zhao

Received: 9 December 2025
Revised: 16 January 2026
Accepted: 26 January 2026
Published: 29 January 2026

Copyright: © 2026 by the authors. Licensee MDPI, Basel, Switzerland. This article is an open access article distributed under the terms and conditions of the Creative Commons Attribution (CC BY) license.

1. Introduction

While geophysical surveys, like magnetometry or Ground-Penetrating Radar (GPR), and further non-destructive methods are currently standard in archeological research, they are still rarely applied in other fields of heritage protection. There are some published examples on the use of GPR to investigate bricked-up windows and arches [1–3] or to document damage, mainly caused by moisture intrusion, at historic buildings [3–6]. In

contrast, three-dimensional methods like laser scanning (Light Detection and Ranging, LiDAR) or Structure-from-Motion (SfM) are quite often reported in the field of heritage protection to map entire historic buildings [7–10] or single pieces of equipment [11–14]. Our research project on the cathedral of Bamberg includes two geophysical methods, i.e., high-frequency GPR and magnetic susceptibility (MS) prospections, to investigate a medieval bishop's sarcophagus, including its layout, type of construction, and interior design. Specific research questions were the thickness of the stone slabs and a potential internal metal sarcophagus for the actual bones. Without our non-destructive surveys, both targets could only be clarified by opening the sarcophagus, an attempt that is time-consuming, expensive, and not compatible with heritage protection.

Furthermore, there have been recent developments in digital techniques for documenting cultural heritage in a low-cost and efficient way. This works especially well in cases where standard geomatic surveys by Terrestrial Laser Scanning (TLS) or Close-Range Photogrammetry (CRP) fail due to limited spaces or when only individual equipment objects are relevant. Besides the photogrammetric approach using 360-degree cameras [15–17], the built-in LiDAR sensor in Apple devices can be utilized for these attempts [18,19]. We applied the latter method to generate a 2.5D model of the sarcophagus to obtain an impression of the outer layout, potential damage areas, and decoration. This model can also be used to better visualize the geophysical data.

Additionally, material analysis via X-ray fluorescence (XRF) was used to solve some unclear issues where the two geophysical measurements gave contradictory results. Until now, XRF has mainly been applied in heritage protection and art history to analyze the material composition of old paintings [20–25] or archeological findings and objects [26–30]. Therefore, the presented results open another field of application that has not been covered very often.

Such multi-method approaches, analyzing various physical and chemical properties, ensure that the maximum knowledge is gained about the survey object without the necessity of invasive attempts, like opening or drilling holes, to obtain an impression of the inside of such a sarcophagus. This is in line with the principles of sustainable heritage protection, which aims to preserve the relevant sites and objects for future generations.

2. Site Description

Bamberg, a major city in Upper Franconia, a department of Bavaria (Germany), is located approximately 50 km north of Nuremberg near the northern boundary of Bavaria (Figure 1a). It is situated in the northern Regnitz basin and is surrounded by the *Franconian Alb* in the east, the *Hassberge* mountains in the north, and the *Steigerwald* forest in the southwest [31]. The cathedral of Bamberg can be found on top of the central hill among a range of hills along the left bank of the Regnitz River (Figure 1b). On top, an oval-shaped plateau of 470 m length and 250 m width protrudes ca. 20 m above the historic city centre. The geological subsurface is formed by water-impermeable *Oberer Burgsandstein* that is characterized by an alternating layering of sandstone and clay [31,32]. At the Cathedral Hill, it occurs in approximately 150 cm depth, as archeological excavations have revealed [32].

As early as the early medieval period, the hill was settled with a fortress, the so-called *castrum Babenbergh*, whose remains were uncovered by several archeological excavations. During this time, a small church existed at the position of the present cathedral [33–35]. The Diocese of Bamberg was founded in 1007 by the Emperor Heinrich II [33,35]; therefore, it is among the oldest dioceses in Germany. In the same year, the construction of the cathedral started, and it was consecrated in 1012. After several destructive fires, it was rebuilt in 1185 in a Romanesque architectural style, in which it has been preserved [33–35] (Figure 2).

Bishop Gunther descended from the Ekkehardiner dynasty, the margraves of Meissen in Saxony [36], and had been chancellor under Emperor Heinrich II before he became bishop of Bamberg in 1057 [37]. On 23 July 1065, he died in Ödenburg (Sopron, Hungary) on his way back from the Holy Land [36,38]. Among his merits was the formation of the collegiate St. Gangolf in Theuerstadt, a suburb of Bamberg beyond the outer arm of the Regnitz River [37,39].

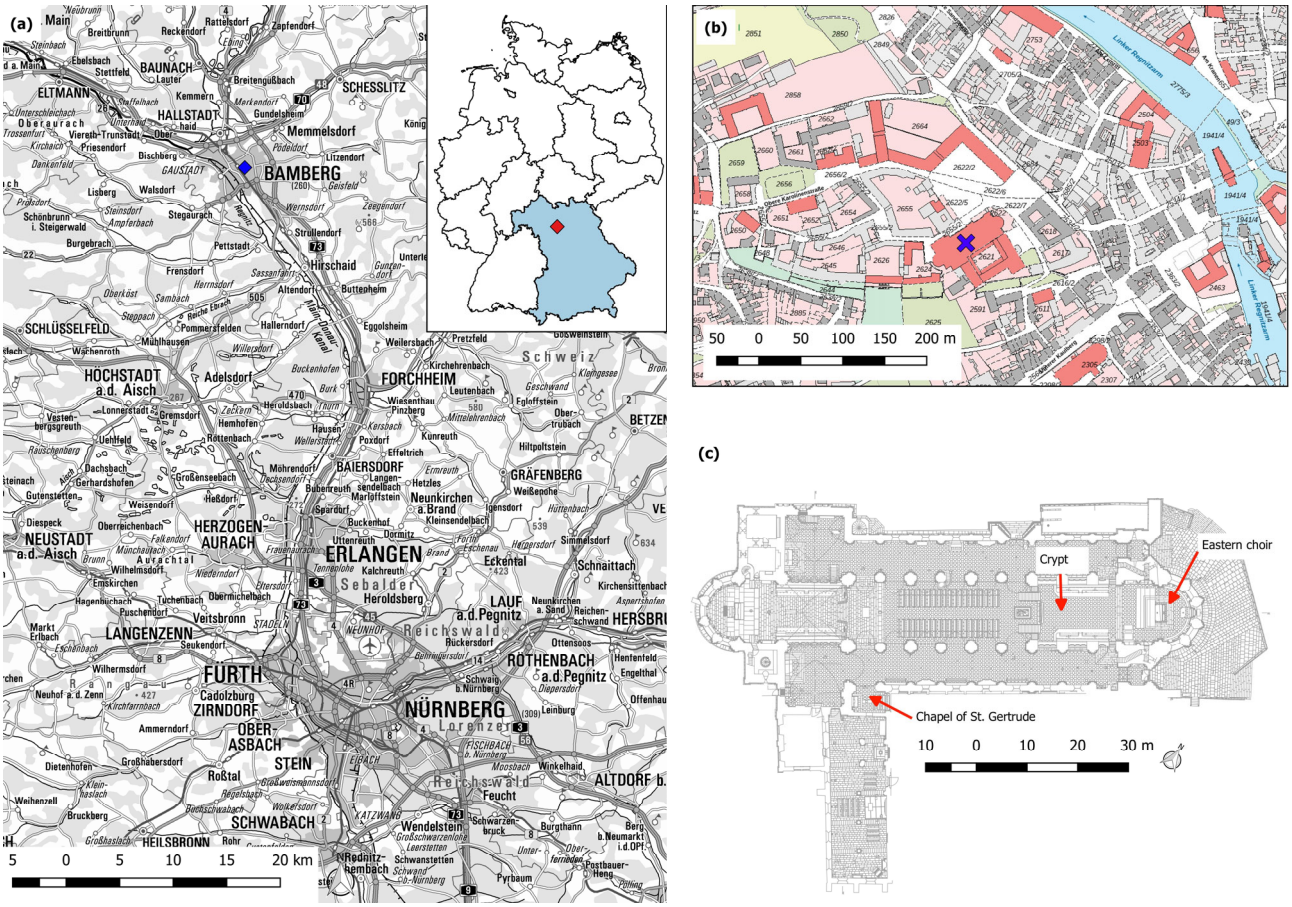

Figure 1. (**a**) Topographical map showing the location of Bamberg within Germany (red rectangle in top right corner; © Bundesamt für Kartographie und Geodäsie, Frankfurt am Main, 2011) and Bavaria (blue rectangle in main map; (© Bayerische Vermessungsverwaltung 2025—www.geodaten.bayern.de). (**b**) Location of the cathedral within the city centre of Bamberg (© Bayerische Vermessungsverwaltung 2025—www.geodaten.bayern.de). (**c**) Map of the Romanesque cathedral with marking of the Chapel of St. Gertrude, the eastern choir, and the crypt (Church's map: © University of Bamberg).

Bishop Gunther was previously buried in front of the Altar of St. Gertrude that he had founded during his reign [38,39] (Figure 1c). In the 14th century, the sarcophagus was verified in the eastern choir, and it can be assumed that it was already transferred to this place of honour in the course of the reconstruction of the cathedral in 1185 [38] (Figure 1c). However, this location was quite obstructive, as the sarcophagus was too close to the altar steps; thus, in 1826, a translocation was planned. In preparation for this procedure, the sarcophagus was opened for the first and last time on 22 December 1830, and in addition to the bones of Bishop Gunther, a decorated burial cloth and a crucifix were found. Furthermore, it was recognized that the corpse of the tall bishop would not have fit into the narrow sarcophagus. Hence, it is safe to assume that he was buried somewhere else in the beginning, and his bones were later transferred into this sarcophagus [36,38].

These modern studies contradict the assumptions of Reitzenstein [39], who postulated that Bishop Gunther was originally buried there. Since 1934, the sarcophagus of Bishop Gunther has been on display in the eastern crypt of the Bamberg Cathedral [36,38,39] (Figure 1c).



Figure 2. Aerial photo of Bamberg Cathedral integrated into the surrounding historic monuments. View from west (BLfD Aerial photo archive, Photographer: Klaus Leidorf, Date: 4 May 2023, Archive-no. 6130/014, Photo-no. R5018663).

3. Survey Equipment

3.1. LiDAR

Light Detection and Ranging (LiDAR) is usually a remote sensing technology using the travel time of laser light to precisely calculate the distance to an object of interest. However, in this case, LiDAR refers specifically to a certain gadget; Apple Inc. (Cupertino, CA, USA) provided its iPhone 12 Pro and iPad Pro 4th generation and all succeeding models with the so-called LiDAR scanner (Figure 3). It was initially designed to improve augmented reality applications [40,41] and allows the generation of 3D models by combining the spatial information of the scanner and the colour information of the camera. Besides the 5 m operation range, Apple Inc. does not provide any official information about the used technology or accuracy. However, System Plus Consulting by Yole Group has conducted a reverse engineering analysis, which allows for some insight: the LiDAR scanner consists of a vertical-cavity surface-emitting laser (VCSEL) as an emitter with a 940 nm wavelength NIR-pulse and a single-photon avalanche diode (SPAD) array as a detector. The sensor features 10 µm-long pixels and a resolution of 30 kilopixels [41]. This focal length is equivalent to the 26 mm of the main 12-megapixel camera of the iPad and iPhone [42]. Several field tests indicate that the manufacturer-indicated 5 m range applies under laboratory conditions and most indoor measurements; however, under field conditions, the point density decreases logarithmically with distance, and the maximum range can diminish to 2–3 m [42,43].



Figure 3. Photo of an iPhone LiDAR sensor. The smartphone is mounted in a carrying frame for easier scanning of the object (Photo: Roland Linck).

Furthermore, a sufficient accuracy and object detection can only be reached above a threshold of 10 cm. Above that value, the average accuracy lies within the centimetre range, reaching minimum values of ±1 cm depending on field conditions, measurement principles, and the applications used [19,42–44].

The LiDAR scanner can be used with various free-of-charge or commercial applications to generate 3D models; here, we used the free Scaniverse App V5.1.0 [45].

3.2. Ground-Penetrating Radar

The method of GPR is based on the transmission of electromagnetic waves into the subsurface. At material discontinuities or varying materials, some portion of the transmitted waves is reflected back to the instrument and recorded by a receiver antenna. The details on the methodology of GPR are comprehensively described in a multitude of textbooks [46–48] and will not be discussed further here. GPR is one of the best choices among the geophysical prospection methods to investigate air-filled structures like the medieval sarcophagus, as there is a strong reflection contrast between stone and air [47,49–51].

For the investigation of the sarcophagus of Bishop Gunther, two high-frequency GPR systems, originally designed for mapping steel reinforcement within concrete, were applied: a GSSI StructureScan Mini XT (Nashua, NH, USA) with a centre frequency of 2.7 GHz (Figure 4a) and a Sensors & Software Conquest 100 (Mississauga, ON, Canada) with a centre frequency of 1 GHz (Figure 4b). For the first instrument, the so-called Palm antenna was attached to the equipment, as, due to its smaller size, it could be operated more easily along the narrow side slabs. Both surveys were executed on parallel lines with 5 cm spacing on all four sides of the sarcophagus, roughly parallel to the ground. The profiles were marked with a fixed grid printed on a truck tarpaulin. The cover plate of the sarcophagus could not be mapped due to the relief of the bishop. In addition, no cross-grid survey with perpendicular profiles could be executed, as the cover plate and the pedestal protrude outwards and prohibit a proper antenna contact to the stone plates in the vertical direction for most of the area.

The gridding of the single profiles and the data processing were executed in the proprietary software packages by the instrument manufacturers: for the GSSI data, RADAN 7 [52] was used; for the Sensors & Software data, we applied EKKO_Project 6 [53]. Both allow only a rudimentary processing workflow for these instruments that is not fully

comparable to standard GPR surveys (see Table 1). For the time-to-depth conversion, a standard velocity of 0.1 m/ns was chosen, and no specific hyperbola fitting was applied, as corresponding trial tests revealed that this step was not necessary for collapsing the diffraction hyperbolas.

Table 1. Applied GPR processing steps.

Sensors & Software Conquest 100	GSSI Structure Scan Mini XT
Background Subtraction Dewow Filter Envelope FK Migration	Background Removal 1D Kirchhoff Migration



(**a**) (**b**)

Figure 4. GPR equipment applied for the investigation of the sarcophagus: (**a**) GSSI StructureScan Mini XT with a Palm-antenna; (**b**) Sensors & Software Conquest100. Both photos also visualize the survey setup with a pre-marked grid foil to guarantee exactly parallel profiles and to prevent damaging the sarcophagus surface (Photos: Johanna Skrotzki).

3.3. Magnetic Susceptibility Prospection

For measuring the magnetic volume susceptibility, the Kappa Meter SM30 by ZHinstruments (Brno, Czech Rebublic) was applied (Figure 5). It operates at an oscillator frequency of 8 kHz, has a pickup coil with a diameter of 50 mm, and takes about five seconds for each measurement. Approximately 90% of the signal originates from the half-space about 50 × 20 mm below the coil.

Magnetic volume susceptibility κ describes a proportionality constant defined by the ratio of magnetization M to magnetic field strength H. As a ratio, susceptibility is therefore physically dimensionless in the SI system of units used for all values of magnetic susceptibility presented here. All materials respond to magnetic fields. In the simplest case of

constant MS, one distinguishes diamagnetic, paramagnetic, and ferromagnetic or ferrimagnetic substances. For example, copper, lead, gold, and bronze are diamagnetic and show negative magnetic susceptibility values. Negative values represent materials that counteract the external magnetic field, while positive values strengthen the overall magnetic field. Ferromagnetic materials, such as iron, nickel, and cobalt, show very high positive κ-values. Ferrimagnetic mineral iron oxides, such as magnetite, maghemite, or titanomagnetite, show high positive magnetic susceptibility values, whereby antiferromagnetic iron minerals, such as goethite and haematite, produce intermediate magnetic susceptibilities [54,55]. Our device measures the MS of sediments and rocks with a sensitivity of $\pm 1 \times 10^{-7}$ SI units, meaning that magnetite in rocks or sediments can be detected even at a volume concentration of less than 0.002% by volume. Ferromagnetic iron, if present, should produce a clearly measurable positive signal even at a distance of 10–20 cm from the measurement coil. Further details on the methodology can be found, e.g., in [56–58].



Figure 5. Photo of ZHinstruments SM30 used for the first in situ susceptibility survey of the sarcophagus (Photo: Jörg W.E. Fassbinder).

For our measurements on the sarcophagus, a paper template with a measurement grid of 10 × 10 cm was placed on the stone slabs. The measurements were taken at the centre of each measurement square. Due to the point-based sampling, in contrast to GPR, the outward-bending pedestal could also be partly covered. The results were processed and visualized using the programmes Geoplot (Geoscan Ltd., Bradford, UK) [59] and Surfer (Golden Software, Golden, CO, USA) [60] with processing steps similar to those used for magnetometer prospecting data. Negative, i.e., diamagnetic values, appear in light grey–white, while positive values caused by ferri- or ferromagnetic parts are displayed as dark grey–black anomalies.

3.4. X-Ray Fluorescence

X-ray fluorescence (XRF) is a non-destructive analytical technique used in archaeometry to determine the elemental composition of a material. In an XRF measurement, the sample is exposed to a primary X-ray source, which irradiates the atoms in the material. When the atoms absorb this energy, their electrons become excited and are ejected from their shells. As a result, electrons from higher energy levels fall into the vacancies, releasing secondary (or fluorescent) X-rays with characteristic energies specific to each element. By detecting and analyzing these emitted X-rays, the elemental composition of the sample can be identified and quantified [61,62].

For the measurements in Bamberg, the portable X-ray fluorescence spectrometer Bruker Tracer 5G (Billerica, MA, USA) was used (Figure 6). The device is equipped with a rhodium anode as X-ray source, which allows a variable accelerating voltage from 5 kV to 50 kV at a maximum tube current of 200 µA. A silicon drift detector (SDD) with a 1 µm-thick graphene window serves as the detector. To optimize the measurements, particularly the signal-to-noise ratio, an aluminum–titanium filter was placed in front of the detector.

The survey comprised 40 single points in four horizontal rows of varying height at the sarcophagus. Each row consisted of 10 points evenly distributed around the object. The heights were chosen in a way that two rows were located within the diamagnetic part, and the other two were located in the paramagnetic one, which could be separated based on the MS survey data (see Section 4.2). The survey parameters set for the sarcophagus are mentioned in Table 2.



Figure 6. Photo of XRF survey with the Bruker Tracer 5G (Photo: Roland Linck).

Table 2. Overview of the XRF survey parameters.

Phase	1
Survey time [s]	60
Accelerating voltage [kV]	40
Tube current [µA]	11
Filter	Ti25 µm:Al300 µm
Collimator lens [mm]	8

4. Results and Discussion

4.1. LiDAR

The sarcophagus of Bishop Gunther was scanned with iPhone LiDAR from all sides to generate a high-quality 2.5D model of the artefact (Figure 7). This served as a base to visualize the GPR and XRF data acquired in 2025. It could not be used for the MS data that was already measured in 2011. The monument is constructed from several slabs consisting of sandstone and has a height of 60 cm in total. The cover plate dating to 1230 AD has a size of 189 × 65 cm [38].

The motif of the cover plate is a bas-relief of the standing bishop as a full figure, turned to the left in profile (Figure 8). The right hand is raised to a blessing gesture, the left one holds the crook. A Latin inscription is carved in Romanesque capital letters around the circumference, beginning at the top centre and being read as: "† PRESV/L GUNTHERVS VT EVM DONIS PRECE CLERVS/ADDIVET/HORTATVR CVI MVLTA DEDISSE PROBA/TUR" (translated to English: Bishop Gunther urges that the clergy, whom he <once> demonstrably enriched, <now in turn> support him with <their> intercession and gifts.) [37,38,63]. This cover plate depicts one of the most prominent witnesses of the Bamberg sculpture workshop that also created the touristically famous pope statue in the cathedral [38].

Each of the two long sides is formed by two slabs of varying length: the northern one consists of plates of 52 cm (left) and 126 cm (right); the southern one consists of two plates of 89 cm in length (Figure 8). The northern long side and both small sides are decorated with flat concave hollowed reliefs: the north side shows two pigeon-like pairs of birds above a rose, and a full rose bush at the longer slab in between. The head of the sarcophagus (western side) shows two cranes with intertwined necks, and the foot (eastern side) shows a four-legged animal, perhaps a lion with a raised right forefoot. The pigeons and the rose bushes can be interpreted as motifs of the Paradise, whereas the lion and cranes stand for the virtues of Bishop Gunther, namely strength and justice [39,63]. The dating of the reliefs is unsure; possibly, existing slabs were reused [38,39,63]. The reliefs still show traces of paint from various periods, including remnants of a polychrome medieval lead white coating over an initial coating in chalk technique [38]. Such "negative" relief motifs are quite rare, and, according to Müller and Müller [63], they possibly were completely filled with paint to create the effect of a Byzantine enamel of the 10th/11th century. Reitzenstein [39] also deduces the motifs of the slab's reliefs from the Persian–Islamic cultural field, as they lack correspondence in the art of early medieval Europe.

The southern side slab is undecorated (Figure 8). The reason could be that the sarcophagus originally stood against the wall on this side; hence, no decoration was necessary [39,63]. The lower part of the monument consists of a slightly profiled base that, like the cover slab, dates younger, to the 13th century [38,39]. The upper edges of the stone slabs are partly broken out and have iron embeddings at regular distances. These remnants could, under the assumption of a secondary use, indicate that they originally served as a plinth covering of a grating [38].

The raw mesh in Figure 7b illustrates the above-mentioned hollowed reliefs. These can be identified in the data, but they are not very detailed, as this exceeds the resolution of the iPhone LiDAR. To generate a better resolution, a near-field SfM survey would be necessary. However, such a detailed model was not required here, as it only serves as a base to visualize the survey data.



(**a**)

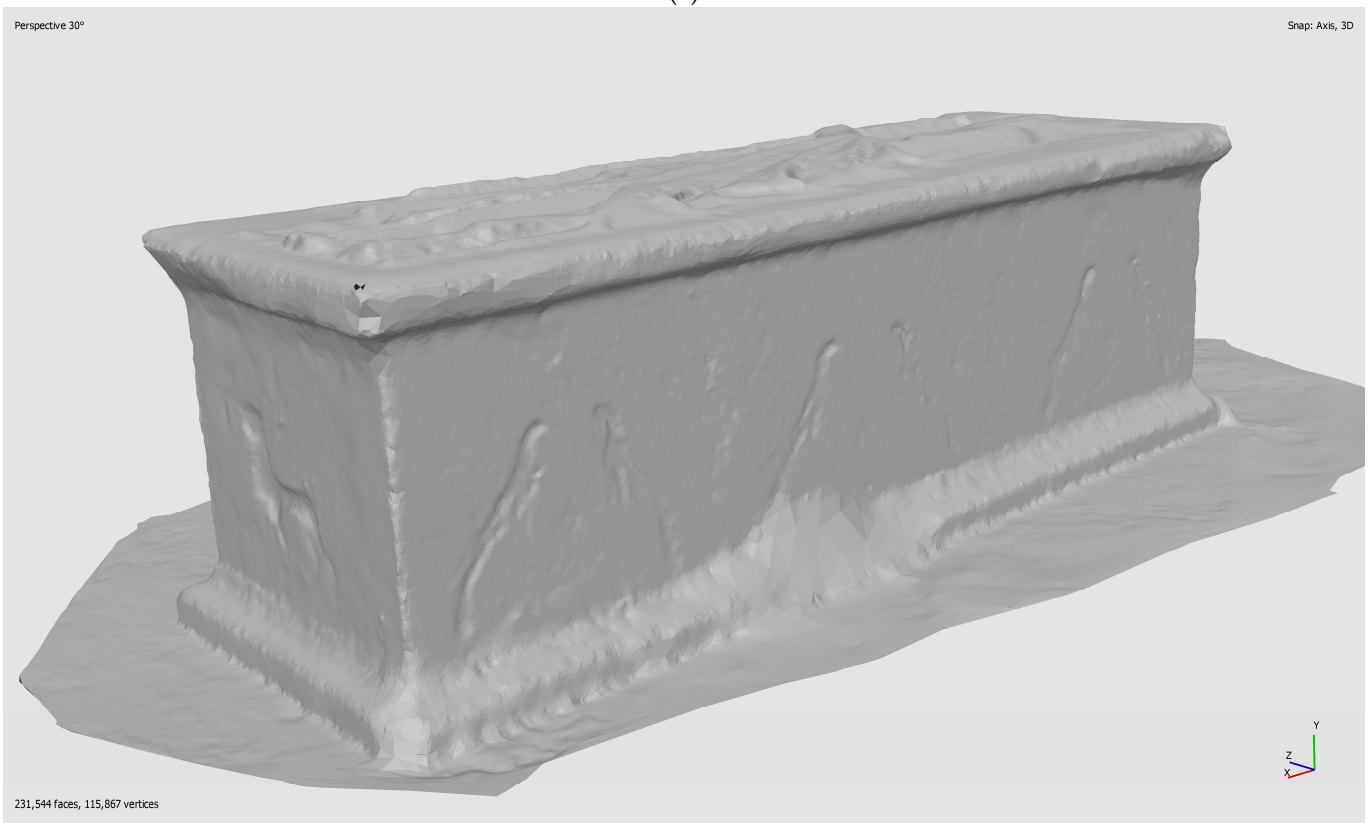

(**b**)

Figure 7. iPhone LiDAR-based 2.5D model of the sarcophagus of Bishop Gunther, view from northeast: (**a**) textured model; (**b**) raw mesh showing the hollowed reliefs at the side slabs. The white marks flag the fixed points of the GPR grid.



Figure 8. An exploded assembly drawing generated from the 2.5D model of all parts of the sarcophagus of Bishop Gunther.

4.2. First Magnetic Susceptibility Measurements

As a first non-destructive geophysical survey, we already executed an MS prospection in 2011. The aim of the study was to investigate whether further hints on the interior of the sarcophagus of Bishop Gunther could be seen and whether any new information on the original use of the sandstone slabs, before they were turned into a grave monument, could be gathered. All four sides were measured at a point spacing of 10 × 10 cm and visualized using digital image processing. This resulted in two grids of 180 × 50 cm for the long sides and two grids of 60 × 50 cm for the short sides. The cover plate was excluded from the surface measurement due to its uneven relief.

The MS of the undisturbed sandstone of the sarcophagus shows average paramagnetic values of $(0.200 \pm 0.020) \times 10^{-3}$ SI units. Individual values from flat areas did not show any anomaly compared to the average value of the sandstone of the side slabs. From the bottom up to a height of about 20 cm, measurement values ranged from $(-10$ to $-0.25) \times 10^{-3}$ SI units (Figure 9). The variation in MS values is slightly higher for the three sides with hollowed motifs (i.e., north side, foot, and head). These negative anomalies indicate a diamagnetic material (e.g., copper, lead, or bronze) being present inside and in the lower part of the sarcophagus. At the time, we proposed the existence of an inner lead coffin inside the sarcophagus as an interpretation [64]. At a few locations, isolated positive values of $(5$ to $10 \pm 2) \times 10^{-3}$ SI units were found. Due to this ferromagnetic behaviour, they indicate iron remnants of the former use of the slabs. However, no further clues on the purpose of primary use can be derived.

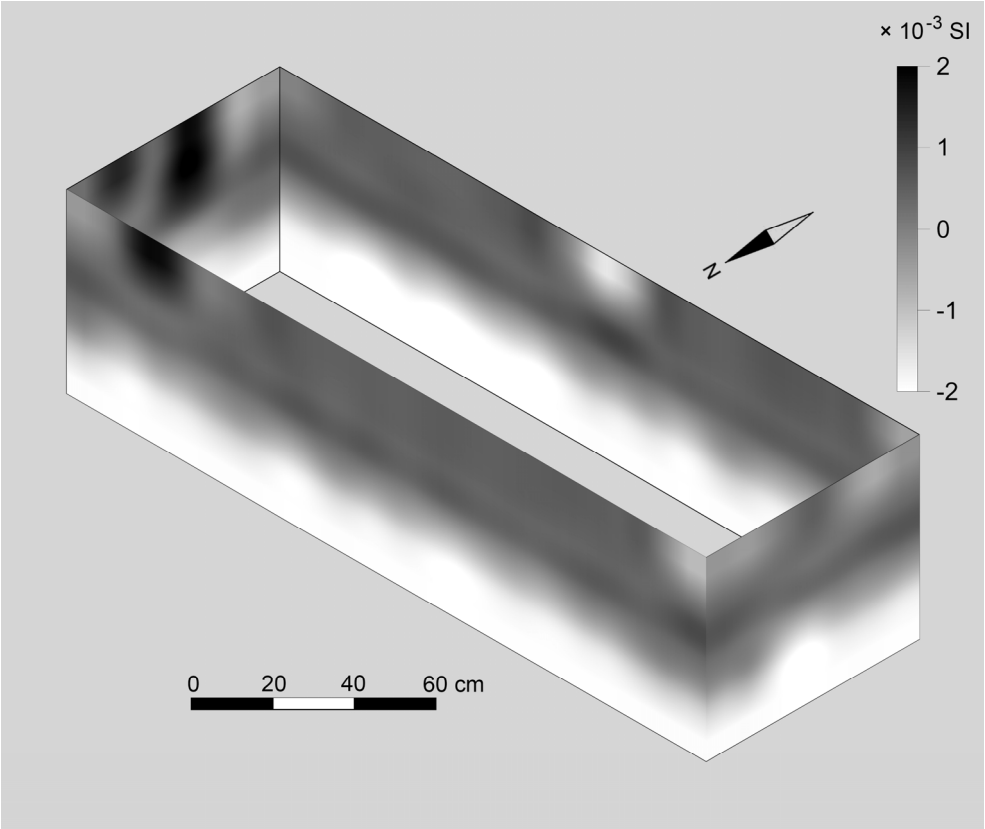

Figure 9. Magnetic susceptibility values in a greyscale visualization of all four slabs of the sarcophagus.

4.3. Ground-Penetrating Radar (GPR)

In addition to the previously mentioned MS survey, we wanted to verify or negate the thesis of a lead coffin by a GPR survey in spring 2025. Such an internal feature should be detectable very well in the radar data, as metal is a strong reflector for electromagnetic waves. The reason for this new research approach was the 19th-century tradition of a too-narrow internal space [36,38]. If Bishop Gunther was not originally buried inside, there would be no mandatory need for a lead coffin. As the GPR data should give detailed information on the slabs' thickness, the available space can be estimated. In total, we measured a 165 × 30 cm grid on each long side (i.e., north and south) and a 45 × 30 cm grid on the short sides (i.e., east and west). To gather as much information as possible, two different high-frequency antennas were applied.

The GPR data of both instruments show a distinct material boundary in approximately 8 cm depth that can be interpreted as the transition from sandstone to air. Similar observations associated with a phase reversal in the GPR data can be found in [65–67]. The depth slices in Figure 10 reveal totally different reflection conditions above and below this depth value: whereas the shallower part is characterized by several small reflections due to internal features in the sandstone, the deeper one is quite homogeneous. The profile view in Figure 11 shows hyperbolic branches in ca. 8 cm from each end of the profile, indicating the thickness of the adjacent short sides of the sarcophagus. The small internal reflection anomalies in the presumed air-filled central part are possibly caused by remains of the bishop's bones, as it is not documented whether these were also removed together with the grave findings in 1830.

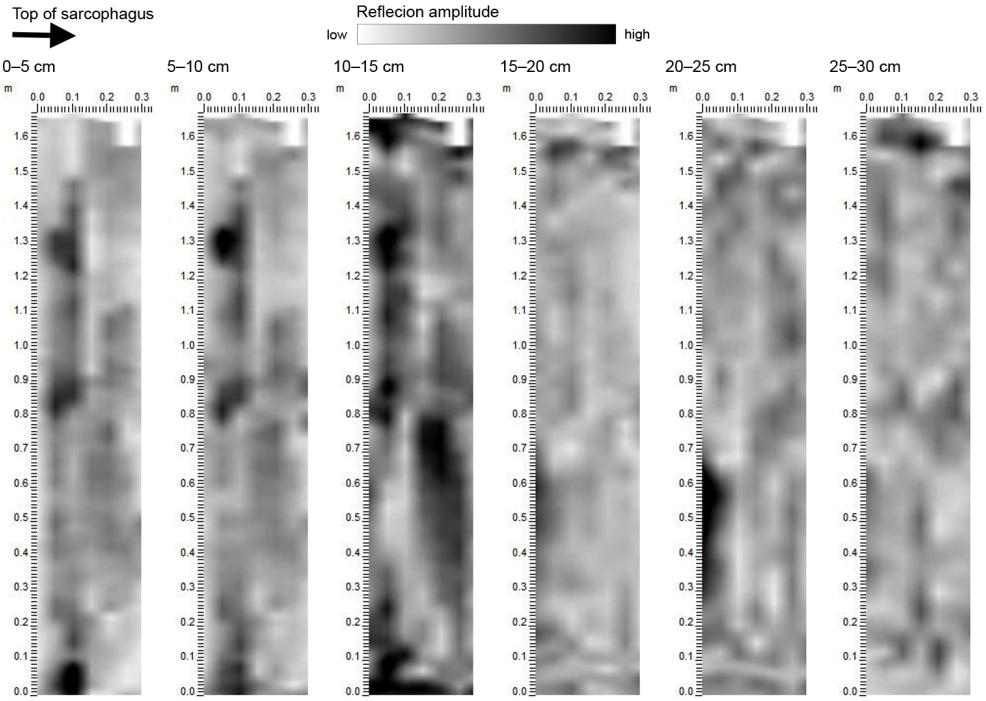

Figure 10. Selection of GPR depth slices of Sensors & Software Conquest 100 showing the varying reflection conditions above and below 10 cm depth. The figure shows the data of the southern slab. Sample interval: 1 × 5 cm, frequency: 1 GHz.

The lower-frequency instrument (i.e., Sensors & Software Conquest 100) was able to penetrate fully through the whole width extent of the sarcophagus at least for the long sides, as there is a significant signal noise detectable in more than 60 cm depth (Figure 11). The noise is caused by external sources of the same frequency due to the location of the site inside the city centre of Bamberg, with, e.g., a lot of mobile phones in the surroundings. The high-frequency GSSI StructureScan Mini XT could not penetrate as deeply, the signal/noise ratio becomes worse after 40 cm depth, and no deeper-lying data can be evaluated.

The GPR depth slices show no correlation with the material differences registered in the MS survey, and the upper part of the slabs has a similar reflection characteristic to the lower one, with diamagnetic behaviour. In addition, there does not seem to be any variation in the GPR velocity associated with the transition in MS data.

For a better visualization of the thickness of the sandstone plates, the corresponding depth slices are overlain on the 2.5D model in Figure 12. Again, it is recognizable that the slabs have a thickness of 8 cm. This results in a single 30 cm-wide and 150 cm-long air-filled cavity inside the sarcophagus, which is definitely too small for the tall Bishop Gunther. Hence, he was not originally buried there, and his bones were transferred into the sarcophagus later, as the records of 1830 mention.

Furthermore, neither of the two GPR datasets reveals any hint of an inner metal coffin behind the sandstone slabs (Figure 12). Therefore, another explanation for the diamagnetic behaviour of the lower 20 cm of the sarcophagus in the MS measurements has to be found.

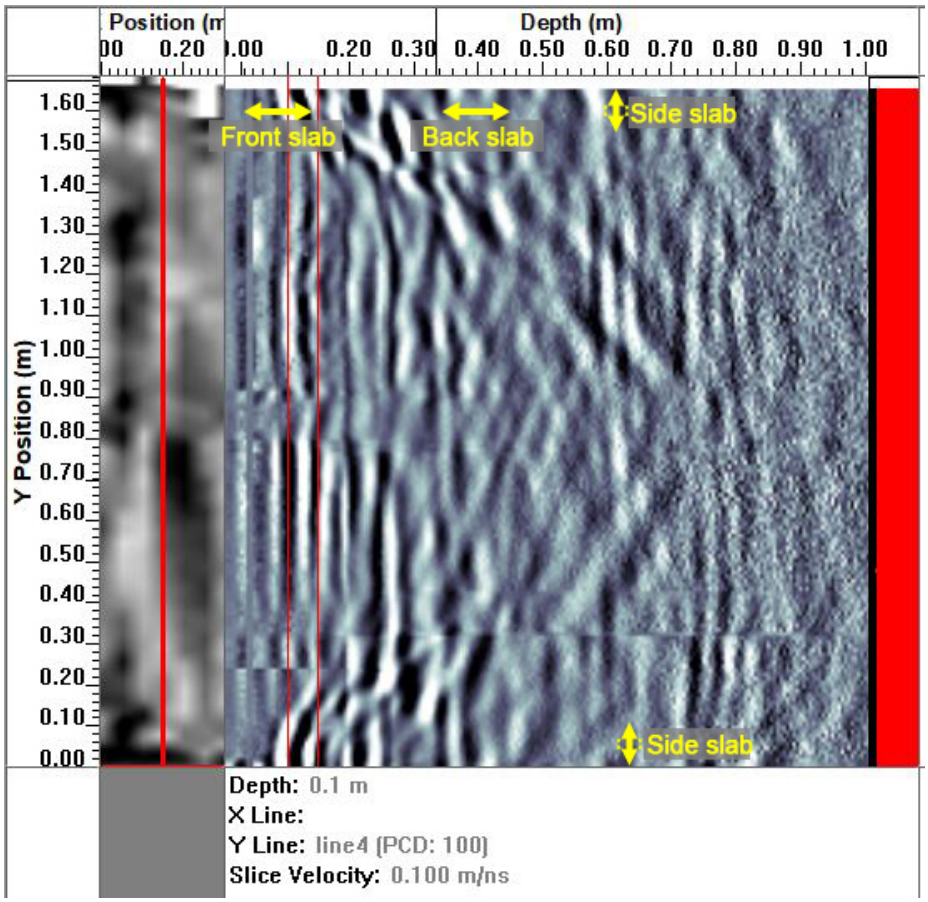

Figure 11. GPR depth slice of the south side (10–15 cm below the surface) and profile view (15 cm from the bottom of the grid) gathered with Sensors & Software Conquest 100. Sample interval: 1 × 5 cm, frequency: 1 GHz.

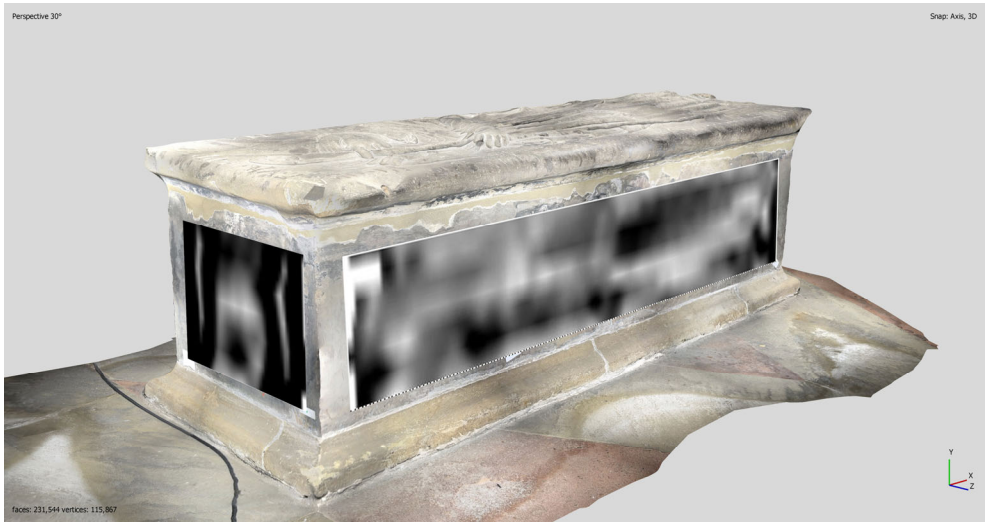

Figure 12. Overlay of the Sensors & Software Conquest 100-based depth slices in 10–15 cm below the surface onto the 2.5D model of the sarcophagus to visualize the slabs' thickness and the absence of any lead coffin that should be prevalent in this depth range. View from the southwest.

4.4. Second Magnetic Susceptibility Measurements

As mentioned in Section 4.1, according to Exner [38], the stone slabs of the sarcophagus are still partly covered by lead white coating remains. Potentially, there was originally much

more coating in medieval times. To test our hypothesis that these lead white colourings could cause the diamagnetic behaviour measured in the first MS data, we tested several samples of modern lead white pigments available in our painting restoration workshop with another MS survey. The result is that, indeed, all of them show a distinct diamagnetic signal (Table 3). The values vary between -33×10^{-3} SI units and -54×10^{-3} SI units.

Table 3. Results of the MS survey of three modern lead white pigments showing the diamagnetic behaviour of all of them. Survey instrument: Bartington MS2K with 2 cm coil size; average of five survey samples.

Name of Pigment and Manufacturer	Magnetic Susceptibility [10^{-3} SI Units]
Kremserweiß, Schachinger (Munich, Germany)	−54.17
Bleiweiß, Kremer (Aichstetten, Germany)	−48.87
Kremserweiß, Kremer (Aichstetten, Germany)	−33.26

Therefore, this apparent discrepancy between the GPR and the MS survey of the sarcophagus in Bamberg could be explained geophysically with this assumption, as the GPR signal was unable to form reflections due to coating remains in the stone slabs. The concentration of diamagnetic lead could possibly be caused by a downward transition of these heavy elements during the several centuries since medieval times, due to the porous structure of the sandstone and the high ambient air humidity in the crypt.

4.5. X-Ray Fluorescence (XRF)

To prove whether there is a significant difference in lead content between the lower 20 cm of the sarcophagus and the upper part due to chemical element precipitation, we executed a chemical analysis via mobile XRF. Since the XRF-radiation in mineral objects such as the outer walls of the sarcophagus has limited penetration depth, primarily surface information should be detected. Elements such as lead (Pb) and copper (Cu) can be reliably identified due to their characteristic fluorescence radiation [68].

To analyze the element distribution depending on the height of the sarcophagus, we set a regular grid of 40 single survey points that could be grouped into ten vertical columns. The location and number of each point can be seen in Figure 13.

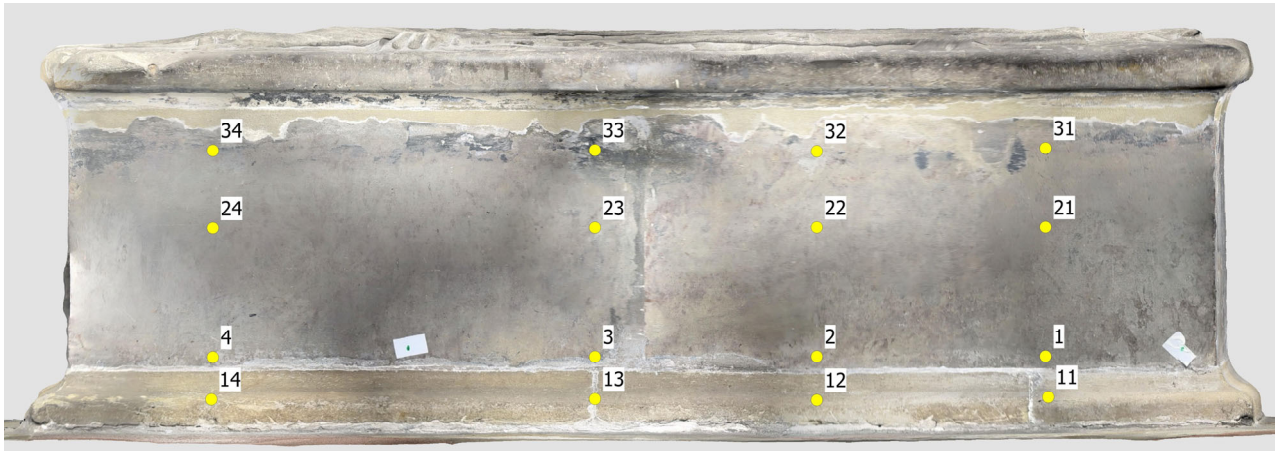

(**a**)

Figure 13. *Cont.*

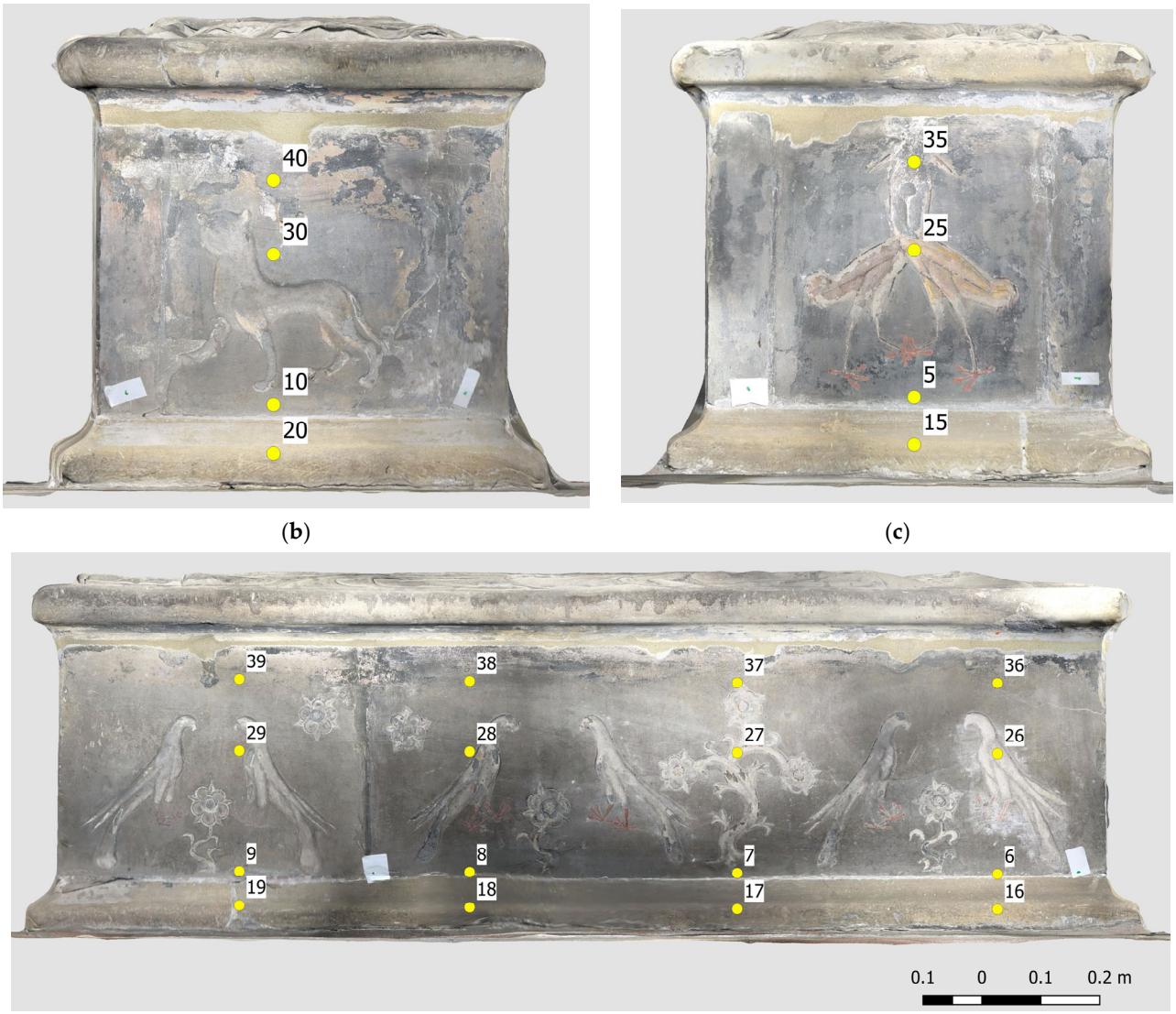

(**b**) (**c**)

(**d**)

Figure 13. Distribution of XRF samples at the sarcophagus: (**a**) southern slab; (**b**) eastern slab; (**c**) western slab; (**d**) northern slab. The sample numbers refer to the text and the following figures.

This makes it possible to more accurately capture the distribution of elements, especially lead. In six measurements (numbers 07, 09, 25, 27, 35, and 40), the visible remnants of the coating, which presumably contained lead white, were measured (Figure 14). Their position, nonetheless, was not changed to an area without remains to maintain the predefined regular grid of survey points.

In nearly all survey points, lead could be detected, confirming that, although in low concentrations, Pb residues are present on the surface. The detected lead signals are generally weak in intensity, but show a certain distribution profile, which is presented in Figure 15, showing the corresponding net values. These are the dimensionless, baseline-corrected surface integrals of the respective element signals that can be used for the relative comparison of two element signals, such as Pb in this case. However, a direct comparison of the net values of different elements and the associated quantification is only possible using material-dependent calibration, as the weighting of the signals (net value) is not congruent with the quantification. Since a mixed material (stone and coating) is present, no absolute statement can be made about the quantification.

As mentioned before, the penetration depth of X-ray radiation in the XRF method is strongly limited—especially in such mineral-dense material like the sarcophagus' sandstone slabs—so only near-surface lead occurrences could be detected. Particularly notable are the six measurement points, 07, 09, 25, 27, 35, and 40, where a significantly increased lead content was found. The highest value was measured at point 25, where lead was detected as the main element (see Figure 15). The high lead levels at these points can be explained by the fact that visible remnants of the paint layer are still present at these locations (Figure 14a). It is likely that this is a lead white-based coating ($2PbCO_3 \cdot Pb(OH)_2$), possibly used as a light primer.

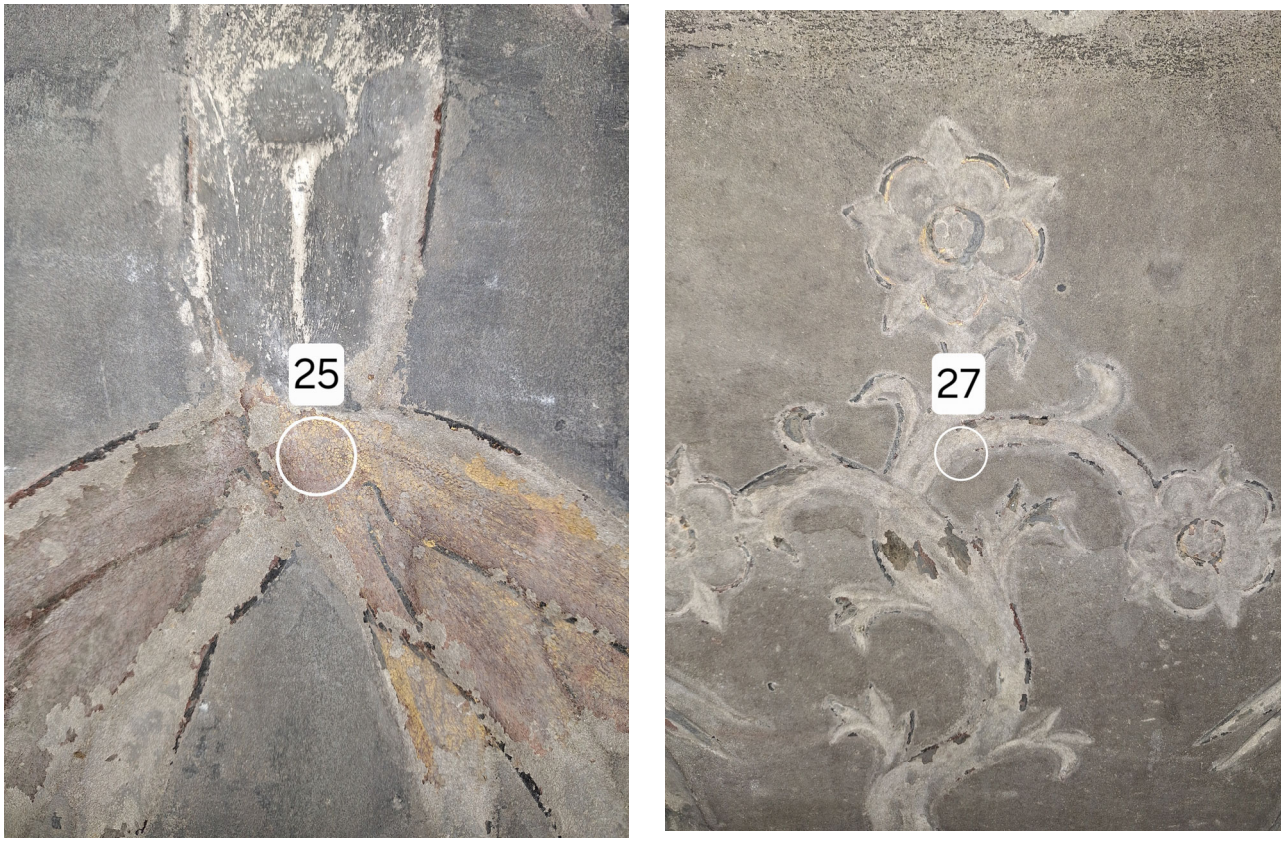

(**a**) (**b**)

Figure 14. Examples of XRF survey points 25 (**a**) and 27 (**b**) showing their location directly at the remains of the lead white coating. For location at the sarcophagus please see Figure 13.

Comparing the remaining spectra without considering the outliers from the visible paint layer, a certain trend in lead distribution can be observed (Figure 15). A comparison of the vertically arranged measurement series shows that higher lead values were generally detected in the lower areas than in the upper areas. The average value of the lower two survey rows is elevated by a factor of 2 compared to the upper ones, which is identifiable in the single spectra per column, e.g., of column 10 at the eastern side (Figure 16). Additionally, differences are not only vertical but also horizontal: the shorter sides (west and east slabs) show higher lead values at all measurement points compared to the southern side. The latter reveals the most homogeneous distribution (Figure 15), as this side has only a few lead white coating remains. The latter are mostly concentrated on the incised motives of the other three sides. Moreover, the same effect is visible in the single MS measurements in the diamagnetic part of the sarcophagus (see Section 4.2). The reason why the MS surveys directly on top of the coating remain do not show distinct peaks is that the instrument measures the volume susceptibility of the 5 cm coil diameter, and hence, over 5 cm depth.

Therefore, the lead content is averaged out in paint remains of less than 1 cm in size and of a few millimetres in thickness. In contrast, the XRF instrument has a measurement window of only 8 mm in diameter and a few millimetres in depth. Thus, distinct peaks can be detected in the case that the coating remains are exactly hit.

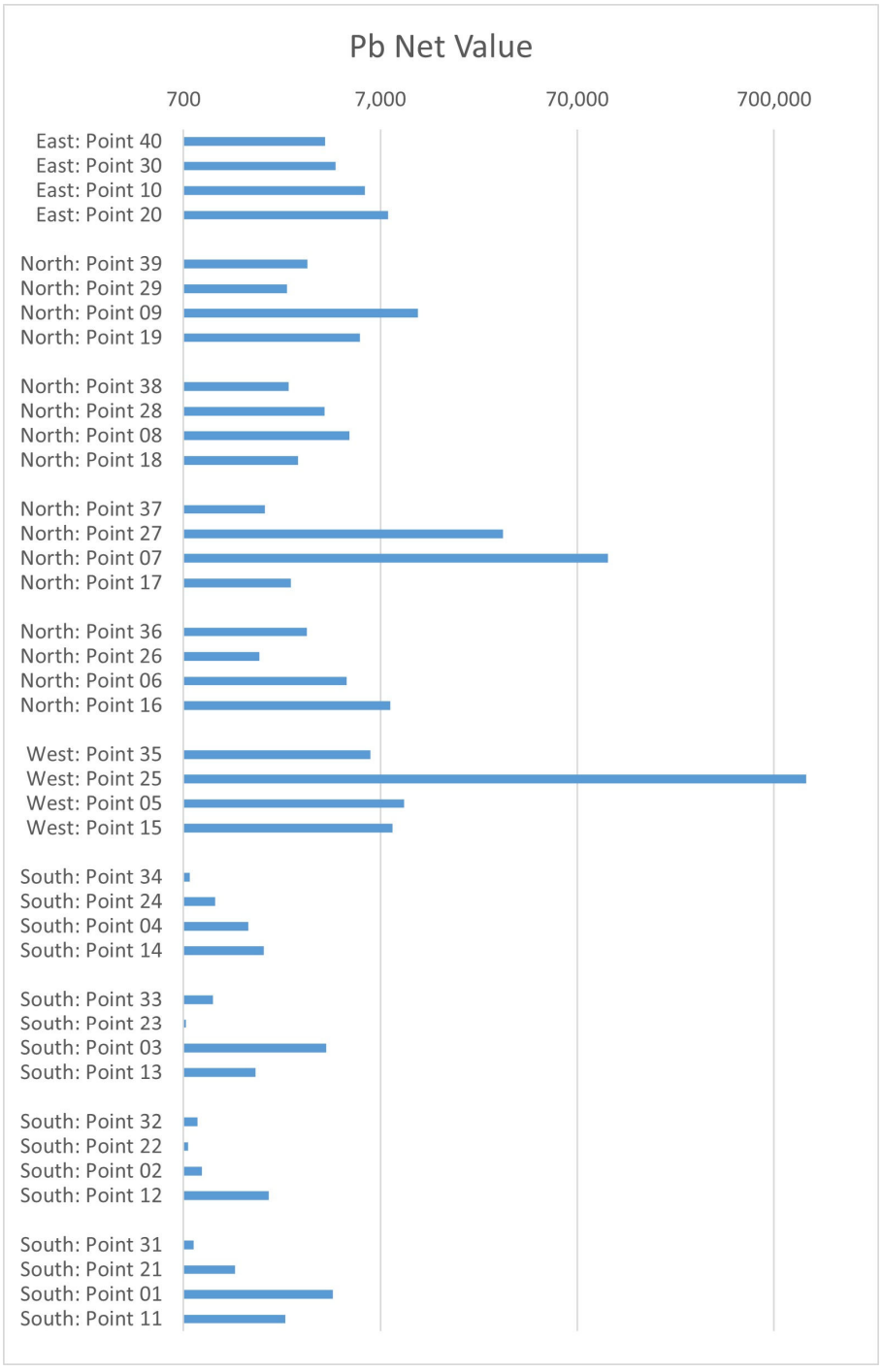

Figure 15. Distribution profile of the element lead based on the respective net values. The scale is logarithmic. The sorting of points is downward for each column. The exact location of the points can be seen in Figure 13.

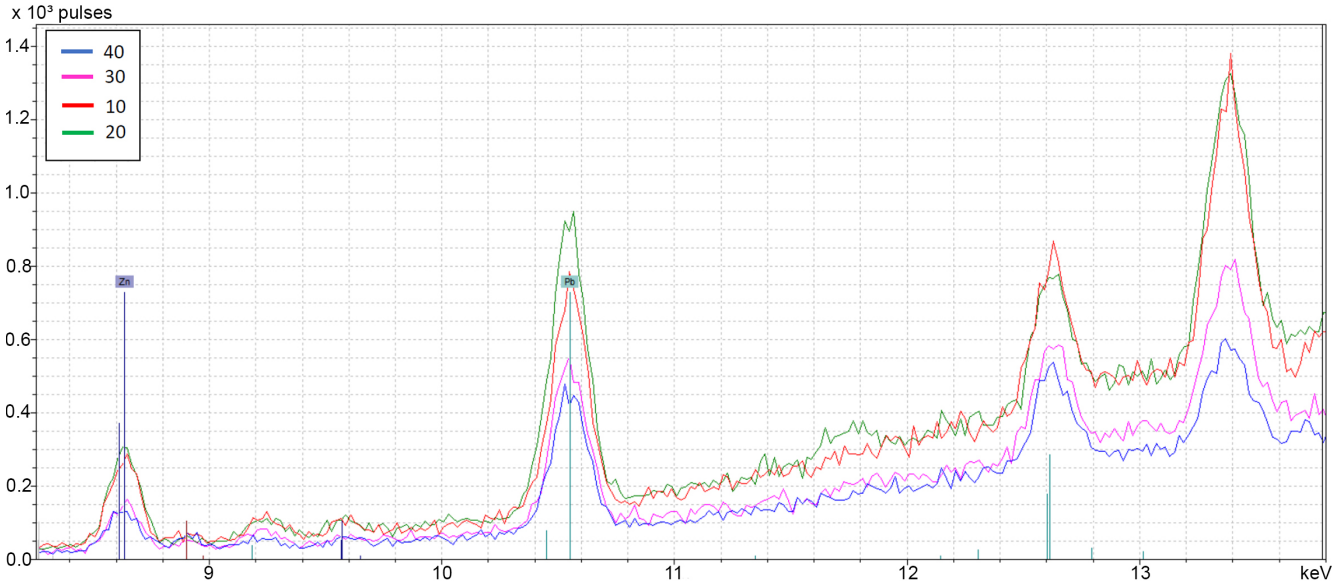

Figure 16. XRF spectra of measurement column 10 containing survey points 10, 20, 30, and 40. To improve visualization, especially of some weaker signals, the spectrum shows a clipped view of the range between approximately 8 keV and 14 keV. The exact location of the points can be seen in Figure 13.

Elevated lead concentrations were also measured with XRF on the northern side. For example, measurement points 28 and 38 in the upper rows show higher lead values than the lower measurement points 04 and 14. This anomaly might also be caused by some metal cramps consisting of lead used to fix the cover plate, or might belong to the first use of the stone slabs. Hence, the differences between the four sarcophagus sides probably cannot be explained solely by the former paint layer, and the high variability of the measurement values suggests that multiple factors could have influenced the distribution of lead. In addition to the use of lead white in the coating, properties of the rock itself—such as naturally occurring lead deposits—could also have affected the measurements. This possibility would particularly explain the irregular fluctuations within the measurement series.

5. Conclusions

The presented results show that a single method is often insufficient to make clear statements; similar discoveries are already published, e.g., by [69–73]. Whereas the assumption of an internal lead sarcophagus inside the stone one seemed reasonable from a geophysical point of view after only executing the MS survey, the GPR data contradicted this hypothesis, as any metal installation behind the stone slabs should show up as a strong reflector. This problem could only be explained after further investigations using XRF. The corresponding results indicate that the diamagnetic behaviour is likely caused by a concentration of lead in the lower part of the sarcophagus. The origin of the element is a former lead white coating with heavy Pb elements slowly diffusing downwards due to the porous sandstone and the high moisture in the crypt. Such a moisture-driven diffusion of lead elements due to corrosion followed by leaching of the paint layer is also mentioned by, e.g., [74,75]. However, the distribution in XRF cannot be attributed solely to this; it is likely that natural material differences in the rock also play a role. The high diamagnetic susceptibility anomaly in the plinth and the lower part of the sarcophagus that was measured could prove the hypothesis of Müller and Müller [63] of completely colour-filled incised reliefs to imitate the effect of Byzantine enamel of the 10th/11th century. Furthermore, the hypothesis that the sarcophagus was attached to the church's wall with its undecorated,

nowadays southern side, is proven by our XRF data, which shows significantly lower values for all survey points compared to the other three slabs.

Via the GPR survey, it was possible to investigate the internal layout of the sarcophagus for the first time. With slab thicknesses of 8 cm, this results in an internal, air-filled space of only 30 × 150 cm. This is far too small for burying a corpse and indicates a later use as a secondary burial monument.

As a final comment, the following can be stated for similar studies: if an investigation of a single physical or chemical parameter is not sufficient, a combination of various methods from different disciplines often helps to solve the problem. This is not only applicable to other sarcophagi but also to other kinds of sealed heritage objects to avoid a destructive opening.

Author Contributions: Project supervision, R.L.; project concept development, R.L. and A.S.; data acquisition, R.L., J.W.E.F., and J.S.; data processing, R.L. and J.S.; validation, R.L., J.W.E.F., and A.S.; writing—original draft preparation, R.L., J.S., and T.H.; writing—review and editing, A.S. and J.W.E.F.; visualization, R.L. and J.S. All authors have read and agreed to the published version of the manuscript.

Funding: This research received no external funding.

Data Availability Statement: The data that support the findings of this study are available from the corresponding author upon reasonable request.

Acknowledgments: First of all, the authors want to thank the diocesan administration of Bamberg, especially Birgit Kastner and her team, for the permit to execute our surveys. We want to thank Arman Moradi Fard (LMU Munich) for his assistance during the GPR survey. In addition, we thank Andreas Müller of the restoration working group of the BLfD for providing us with comparison samples of modern lead white pigments and the scientific discussion about their use in paintings.

Conflicts of Interest: The authors declare no conflicts of interest.

Abbreviations

The following abbreviations are used in this manuscript:

CRP	Close-Range Photogrammetry
GPR	Ground-Penetrating Radar
GSSI	Geophysical Survey Systems, Inc.
LiDAR	Light Detection and Ranging
MS	Magnetic Susceptibility
SfM	Structure-from-Motion
SPAD	Single-Photon Avalanche Diode
TLS	Terrestrial Laser Scanning
VCSEL	Vertical-Cavity Surface-Emitting Laser
XRF	X-ray Fluorescence

References

1. Barraca, N.; Almeida, M.; Varum, H.; Almeida, F.; Matias, M.S. A case study of the use of GPR for rehabilitation of a classified Art Deco building: The InovaDomus house. *J. Appl. Geophys.* **2016**, *127*, 1–13. [CrossRef]
2. Benech, C.; Vitale, Q.; D'Agostino, L.; Parfant, C. GPR Mural Study of the Commandery of Jalès (France). *ArchéoSciences* **2021**, *45–1*, 157–159. [CrossRef]
3. Schang, P.; Benech, C.; Vitale, Q. GPR: New perspectives in building archaeology. *ArchéoSciences* **2025**, *49–1*, 489–492. [CrossRef]
4. Ferrara, C. Detecting Moisture Damage in Archaeology and Cultural Heritage: A Brief Introduction. *Int. J. Archaeol.* **2015**, *3*, 57. [CrossRef]
5. Angelis, D.; Tsourlos, P.; Tsokas, G.; Vargemezis, G.; Zacharopoulou, G.; Power, C. Combined application of GPR and ERT for the assessment of a wall structure at the Heptapyrgion fortress (Thessaloniki, Greece). *J. Appl. Geophys.* **2018**, *152*, 208–220. [CrossRef]

6. Barone, P.M.; Ferrara, C. Non-Invasive Moisture Detection for the Preservation of Cultural Heritage. *Heritage* **2018**, *1*, 163–170. [CrossRef]
7. Yastikli, N. Documentation of cultural heritage using digital photogrammetry and laser scanning. *J. Cult. Herit.* **2007**, *8*, 423–427. [CrossRef]
8. Kwoczynska, B.; Litwin, U.; Piech, I.; Obirek, P.; Sledz, J. The Use of Terrestrial Laser Scanning in Surveying Historic Buildings. In Proceedings of the 2016 Baltic Geodetic Congress (BGC Geomatics), Gdansk, Poland, 2–4 June 2016; pp. 263–268. [CrossRef]
9. Angelini, A.; Cozzolino, M.; Gabrielli, R.; Gentile, V.; Mauriello, P. Three-Dimensional Modeling and Non-Invasive Diagnosis of a Huge and Complex Heritage Building: The Patriarchal Basilica of Santa Maria Assunta in Aquileia (Udine, Italy). *Remote Sens.* **2023**, *15*, 2386. [CrossRef]
10. Elbshbeshi, A.; Gomaa, A.; Mohamed, A.; Othman, A.; Ibraheem, I.M.; Ghazala, H. Applying Geomatics Techniques for Documenting Heritage Buildings in Aswan Region, Egypt: A Case Study of the Temple of Abu Simbel. *Heritage* **2023**, *6*, 742–761. [CrossRef]
11. Hess, M.; Luhmann, T. 3D-Erfassung in der Denkmalpflege: Anforderungen und Perspektiven. In *Meydenbauer, Busch: Pioniere der Photogrammetrie: Begleitband zur Sonderausstellung im Kulturzentrum Rathenow*; Götze, B., Ed.; Deutsche Nationalbibliothek Frankfurt am Main: Frankfurt am Main, Germany, 2021; pp. 58–65. [CrossRef]
12. Verhoeven, G.; Santner, M.; Trinks, I. Bildbasierte 3D-Modellierung der Wandmalerei in der Bischofstorvorhalle im Wiener Stephansdom. *Osterr. Z. Für Kunst Denkmalpfl.* **2012**, *75*, 163–174. [CrossRef]
13. Lanteri, L.; Calandra, S.; Briani, F.; Germinario, C.; Izzo, F.; Pagano, S.; Pelosi, C.; Santo, A.P. 3D Photogrammetric Survey, Raking Light Photography and Mapping of Degradation Phenomena of the Early Renaissance Wall Paintings by Saturnino Gatti—Case Study of the St. Panfilo Church in Tornimparte (L'Aquila, Italy). *Appl. Sci.* **2023**, *13*, 5689. [CrossRef]
14. Linck, R.; Stele, A. Structure-from-Motion-Kartierung ultrafeiner Strukturen am Beispiel der Pressbrokatapplikation in der Memminger Frauenkirche. *Archaeol. Austriaca* **2024**, *108*, 271–282. [CrossRef]
15. Barazzetti, L.; Previtali, M.; Roncoroni, F. Can we use low-cost 360 degree cameras to create accurate 3D models? *Int. Arch. Photogramm. Remote Sens. Spat. Inf. Sci.* **2018**, *XLII–2*, 69–75. [CrossRef]
16. Perfetti, L.; Spettu, F.; Achille, C.; Fassi, F.; Navillod, C.; Cerutti, C. A multi-sensor approach to survey complex architectures supported by multi-camera photogrammetry. *Int. Arch. Photogramm. Remote Sens. Spat. Inf. Sci.* **2023**, *48*, 1209–1216. [CrossRef]
17. Pérez-García, J.L.; Gómez-López, J.M.; Mozas-Calvache, A.T.; Delgado-García, J. Analysis of the Photogrammetric Use of 360-Degree Cameras in Complex Heritage-Related Scenes: Case of the Necropolis of Qubbet el-Hawa (Aswan Egypt). *Sensors* **2024**, *24*, 2268. [CrossRef]
18. Murtiyoso, A.; Grussenmeyer, P.; Landes, T.; Macher, H. First assessments into the use of commercial-grade solid state lidar for low cost heritage documentation. *Int. Arch. Photogramm. Remote Sens. Spat. Inf. Sci.* **2021**, *XLIII-B2-2021*, 599–604. [CrossRef]
19. Losè, L.T.; Spreafico, A.; Chiabrando, F.; Tonolo, F.G. Apple LiDAR Sensor for 3D Surveying: Tests and Results in the Cultural Heritage Domain. *Remote Sens.* **2022**, *14*, 4157. [CrossRef]
20. Alfeld, M.; Pedroso, J.V.; Van Eikema Hommes, M.; Van der Snickt, G.; Tauber, G.; Blaas, J.; Haschke, M.; Erler, K.; Dik, J.; Janssens, K. A mobile instrument for in situ scanning macro-XRF investigation of historical paintings. *J. Anal. At. Spectrom.* **2013**, *28*, 760–767. [CrossRef]
21. Reiche, I.; Müller, K.; Mysak, E.; Eveno, M.; Mottin, B. Toward a three-dimensional vision of the different compositions and the stratigraphy of the painting L'Homme blessé by G. Courbet: Coupling SEM–EDX and confocal micro-XRF. *Appl. Phys. A* **2015**, *121*, 903–913. [CrossRef]
22. Mosca, S.; Frizzi, T.; Pontone, M.; Alberti, R.; Bombelli, L.; Capogrosso, V.; Nevin, A.; Valentini, G.; Comelli, D. Identification of pigments in different layers of illuminated manuscripts by X-ray fluorescence mapping and Raman spectroscopy. *Microchem. J.* **2015**, *124*, 775–784. [CrossRef]
23. Delaney, J.K.; Conover, D.M.; Dooley, K.A.; Glinsman, L.; Janssens, K.; Loew, M. Integrated X-ray fluorescence and diffuse visible-to-near-infrared reflectance scanner for standoff elemental and molecular spectroscopic imaging of paints and works on paper. *Herit. Sci.* **2018**, *6*, 31. [CrossRef]
24. Hradilová, J.; Hradil, D.; Pech, M.; Bezdička, P.; Neděla, V.; Tihlaříková, E.; Targowski, P. Complementary use of X-ray based imaging and analytical methods in the investigation of miniature portraits. *Microchem. J.* **2019**, *153*, 104371. [CrossRef]
25. Wagner, J.; Stege, H. Gemäldeuntersuchungen mittels Makro-Röntgenfluoreszenz-Scanning—Ein Erfahrungsbericht aus den Münchner Pinakotheken. In *Bildgebende Verfahren—Trends und Fallbeispiele zur Zerstörungs-Freien Untersuchung und Erhaltung von Kulturerbe; Arbeitshefte des Brandenburgischen Landesamtes für Denkmalpflege und Archäologischen Landesmuseum Bd. 61*; Brandenburgisches Landesamt für Denkmalpflege und Archäologisches Landesmuseum: Brandenburg, Germany, 2021; pp. 79–93.
26. Calza, C.; Anjos, M.J.; Bueno, M.I.M.S.; De Souza, S.M.; Brancaglion, A., Jr.; Lima, T.A.; Lopes, R.T. XRF applications in archaeometry: Analysis of Marajoara pubic covers and pigments from the sarcophagus cartonage of an Egyptian mummy. *X-Ray Spectrom.* **2007**, *36*, 348–354. [CrossRef]

27. Roberta, I.; Susanna, B.; Emma, C.; Barbara, M. An integrated multimethodological approach for characterizing the materials and pigments on a sarcophagus in St. Mark, Marcellian and Damasus catacombs. *Appl. Phys. A* **2015**, *121*, 1235–1242. [CrossRef]
28. Bracci, S.; Magrini, D.; Manganelli del Fà, R.; Cuzman, O.A.; Mazzei, B. Brightly Colored to Stay in the Dark. Revealing of the Polychromy of the Lot Sarcophagus in the Catacomb of San Sebastiano in Rome. *Heritage* **2020**, *3*, 858–874. [CrossRef]
29. Al Sekhaneh, W.; Mahmoud, G.A.; Elserogy, A.; al-Boorini, B.F. Deterioration and conservation of an archaeological Byzantine lead sarcophagus from Jerash, Jordan. *Conserv. Sci. Cult. Herit.* **2021**, *21*, 221–239. [CrossRef]
30. Van der Perre, A.; Boschloos, V.; Hameeuw, H.; Braekmans, D. A complementary integrated approach using non-destructive optical and X-ray methodologies for pigment characterisation on an ancient Egyptian coffin. *Eur. Phys. J. Plus* **2025**, *140*, 428. [CrossRef]
31. Pfaffenberger, S. *Aspekte der Stadtentwicklung Bambergs im Frühen und Hohen Mittelalter aus Archäologischer Sicht*; Arbeiten zur Archäologie Süddeutschlands Bd. 32; Verlag Dr. Faustus: Duisburg, Germany, 2020.
32. Zeune, J. Die Ausgrabungen am Bamberger Domberg—Ein Vorbericht. *Das Archäologische Jahr Bayern* **1990**, *1991*, 162–163.
33. Winterfeld, D. *Der Dom in Bamberg, Bd. 1: Die Baugeschichte bis zur Vollendung im 13. Jahrhundert*; Gebr. Mann Verlag: Berlin, Germany, 1979; pp. 16–29.
34. Sage, W. Die Ausgrabungen im Bamberger Dom. In *1002–1024—Kaiser Heinrich II*; Kirmeier, J., Schneidmüller, B., Weinfurter, S., Brockhoff, E., Eds.; Veröffentlichungen zur Bayerischen Geschichte und Kultur 44/2002; Haus der Bayerischen Geschichte: Regensburg, Germany, 2002; pp. 93–119.
35. Exner, M. *Stadt Bamberg 2—Domberg, 1. Drittelband: Das Domstift, Teil 1: Baugeschichte, Baubeschreibung, Analyse*; Die Kunstdenkmäler von Bayern IV; Deutscher Kunstverlag: Berlin, Germany, 2015.
36. Paschke, H. Das Domstift zu Bamberg in seinen Bauwendungen, Teil II (B-G). *Stud. Zur Bamberger Gesch. Topogr.* **1972**, *45*, 76–78.
37. Heller, J. *Beschreibung der Bischöflichen Grabdenkmäler in der Domkirche zu Bamberg*; Campe Verlag: Hamburg, Germany, 1827; pp. 10–11.
38. Exner, M. *Stadt Bamberg 2—Domberg, 1. Drittelband: Das Domstift, Teil 2: Ausstattung, Kapitelsbauten, Domschatz*; Die Kunstdenkmäler von Bayern IV; Deutscher Kunstverlag: Berlin, Germany, 2015; pp. 1256–1260.
39. Reitzenstein, A. *Die Geschichte des Bamberger Doms—Von den Anfängen bis zu Einer Vollendung im 13. Jahrhundert*; Prestel Verlag: München, Germany, 1984; pp. 41–48.
40. Apple. Apple Unveils New iPad Pro with Breakthrough LiDAR Scanner and Brings Trackpad Support to iPadOS. 18 March 2025. Available online: https://www.apple.com/newsroom/2020/03/apple-unveils-new-ipad-pro-with-lidar-scanner-and-trackpad-support-in-ipados/ (accessed on 18 March 2025).
41. Yole. Apple iPad Pro LiDAR Module. 2025. Available online: https://medias.yolegroup.com/uploads/2020/06/SP20557-Yole-Apple-iPad-pro-Lidar-Module_flyer.pdf (accessed on 24 March 2025).
42. Luetzenburg, G.; Kroon, A.; Bjørk, A.A. Evaluation of the Apple iPhone 12 Pro LiDAR for an Application in Geosciences. *Sci. Rep.* **2021**, *11*, 22221. [CrossRef]
43. Gollob, C.; Ritter, T.; Kraßnitzer, R.; Tockner, A.; Nothdurft, A. Measurement of Forest Inventory Parameters with Apple iPad Pro and Integrated LiDAR Technology. *Remote Sens.* **2021**, *13*, 3129. [CrossRef]
44. Mokroš, M.; Mikita, T.; Singh, A.; Tomaštík, J.; Chudá, J.; Wężyk, P.; Kuželka, K.; Surový, P.; Klimánek, M.; Zięba-Kulawik, K.; et al. Novel low-cost mobile mapping systems for forest inventories as terrestrial laser scanning alternatives. *Int. J. Appl. Earth Obs. Geoinf.* **2021**, *104*, 102512. [CrossRef]
45. Niantic (2025): Scaniverse. Available online: https://scaniverse.com/ (accessed on 3 December 2025).
46. Reynolds, J.M. *An Introduction to Applied and Environmental Geophysic*; Wiley: Hoboken, NJ, USA, 1997; pp. 681–749.
47. Conyers, L.B. *Ground-Penetrating Radar for Archaeology*; Altamira Press: Walnut Creek, CA, USA, 2004.
48. Milsom, J. *Field Geophysics*; Wiley: Hoboken, NJ, USA, 2011; pp. 185–209. [CrossRef]
49. Von der Osten, H. *Geophysikalische Prospektion Archäologischer Denkmale Unter Besonderer Berücksichtigung der Kombinierten Anwendung Geoelektrischer und Geomagnetischer Kartierung, Sowie der Verfahren der Elektromagnetischen Induktion und des Bodenradars*; Shaker Verlag: Düren, Germany, 2003.
50. English Heritage. *Geophysical Survey in Archaeological Field Evaluation*; English Heritage: London, UK, 2008.
51. Linck, R. *Methodische Untersuchungen zur Weiterentwicklung der Boden-und Satellitenradarprospektion in der Archäologie*; Shaker Verlag: Düren, Germany, 2013.
52. GSSI. RADAN Software. 2025. Available online: https://www.geophysical.com/radan (accessed on 5 December 2025).
53. Sensors & Software: EKKO_Project™ GPR Software. 2025. Available online: https://www.sensoft.ca/products/ekko-project/overview/ (accessed on 5 December 2025).
54. Dearing, J. *Environmental Magnetic Susceptibility Using the Bartington MS2 System*; Chi Publishing: Barcelona, Spain, 1999.
55. Wapler, M.C.; Leupold, J.; Dragonu, I.; von Elverfeld, D.; Zaitsev, M.; Wallrabe, U. Magnetic properties of materials for MR engineering, micro-MR and beyond. *J. Magn. Reson.* **2014**, *242*, 233–242. [CrossRef] [PubMed]

56. Dunlop, D.J.; Özdemir, Ö. *Rock Magnetism: Fundamentals and Frontiers*; Cambridge University Press: Cambridge, UK, 1997.
57. Fassbinder, J.W.E. Magnetometry for Archaeology. In *Encyclopedia of Geoarchaeology*; Gilbert, A.S., Goldberg, P., Mandel, R.D., Aldeias, V., Eds.; Encyclopedia of Earth Sciences Series; Springer: Berlin, Germany, 2023. [CrossRef]
58. Dalan, R.A. Susceptibility. In *Encyclopedia of Geoarchaeology*; Gilbert, A.S., Goldberg, P., Mandel, R.D., Aldeias, V., Eds.; Encyclopedia of Earth Sciences Series; Springer: Berlin, Germany, 2024. [CrossRef]
59. Geoscan: GEOPLOT Version 4.0 for Windows. 2025. Available online: https://www.goldensoftware.com/products/surfer/ (accessed on 5 December 2025).
60. Golden Software: Surfer. 2025. Available online: https://www.geoscan-research.co.uk/Geoplot_4_Data_Sheet_Latest.pdf (accessed on 5 December 2025).
61. Beckhoff, B.; Kanngießer, B.; Langhoff, N.; Wedell, R.; Wolff, H. *Handbook of Practical X-Ray Fluorescence Analysis*; Springer: Berlin, Germany, 2006.
62. Sabbatini, L.; van der Werf, I.D. *Chemical Analysis in Cultural Heritage*; De Gruyter: Berlin, Germany, 2020.
63. Müller, S.; Müller, T. Die Grabtumba des Bischofs Gunther im Bamberger Dom. In *Eberhard Hanfstaengl zum 75. Geburtstag*; Ruhmer, E., Ed.; Bruckmann Verlag: München, Germany, 1961; pp. 10–11.
64. Fassbinder, J.W.E.; Linck, R. Geophysikalische Untersuchungen der Tumben in der Ostkrypta des Bamberger Domes mit dem Kappameter. *Das Archäologische Jahr Bayern* **2011**, *2012*, 137–138.
65. Qawasmeh, H.; Al-Hameedawi, M.M.; Conyers, L. Three-dimension (3D) presentation of a hominid cave using ground-penetrating radar. *ArchéoSciences* **2021**, *45–2*, 91–95. [CrossRef]
66. Linck, R.; Stele, A. GPR survey provides evidence for a bricked cellar underneath a Baroque garden pavilion at Memmingen (Bavaria). In Proceedings of the NSGG Meeting "Recent Advances in Archaeological Geophysics", London, UK, 3 December 2024; pp. 41–44.
67. Linck, R.; Zickgraf, B. "Hic requiescit...": Localisation of a Baroque Crypt through a Combination of Ground-Penetrating Radar and Structure-from-Motion. *J. Multidiscip. Res. New Approaches Data* **2024**, *1*, 35–49.
68. Ritgen, U. *Analytische Chemie I*; Springer Nature: Berlin, Germany, 2019.
69. Scollar, I.; Tabbagh, A.; Hesse, A.; Herzog, I. *Archaeological Prospecting and Remote Sensing*; Cambridge University Press: Cambridge, UK, 1990.
70. Neubauer, W.; Eder-Hinterleitner, A.; Seren, S.; Melichar, P. Georadar in the Roman civil town Carnuntum, Austria: An approach for archaeological interpretation of GPR data. *Archaeol. Prospect.* **2002**, *9*, 135–156. [CrossRef]
71. Gaffney, C.; Gater, J. *Revealing the Buried Past: Geophysics for Archaeologists*; Tempus: New York, NY, USA, 2003.
72. Fassbinder, J.W.E. Seeing beneath the farmland, steppe and desert soil: Magnetic prospecting and soil magnetism. *J. Archaeol. Sci.* **2015**, *56*, 85–95. [CrossRef]
73. Keay, S.; Earl, G.; Hay, S.; Kay, S.; Ogden, J.; Strutt, K.D. The role of integrated geophysical survey methods in the assessment of archaeological landscapes: The case of Portus. *Archaeol. Prospect.* **2009**, *16*, 154–166. [CrossRef]
74. Baricza, Á.; Bajnóczi, B.; Szabó, M.; Tóth, M.; Bendö, Z.; Szabó, C. Deterioration of glazed archictectural ceramics due to environmental factors: A comparative study of two buildings in Budapest. *Carpathian J. Earth Environ. Sci.* **2016**, *11*, 449–462.
75. Gliozzo, E.; Ionescu, C. Pigments—Lead-based whites, reds, yellows and oranges and their alteration phases. *Archaeol. Anthropol. Sci.* **2021**, *14*, 17. [CrossRef]

Disclaimer/Publisher's Note: The statements, opinions and data contained in all publications are solely those of the individual author(s) and contributor(s) and not of MDPI and/or the editor(s). MDPI and/or the editor(s) disclaim responsibility for any injury to people or property resulting from any ideas, methods, instructions or products referred to in the content.